

ARTICLE OPEN

Achieving a high dielectric tunability in strain-engineered tetragonal $K_{0.5}Na_{0.5}NbO_3$ filmsLanxia Hao^{1,2}, Yali Yang^{3✉}, Yu Huan^{4✉}, Hongbo Cheng², Yu-Yao Zhao¹, Yingying Wang¹, Jing Yan¹, Wei Ren³ and Jun Ouyang^{2✉}

Using a modified Landau-Devonshire type thermodynamic potential, we show that dielectric tunability η of a tetragonal ferroelectric film can be analytically solved. At a given electric field E , η is a function of the remnant polarization (P_0^f) and the small-field relative dielectric permittivity (χ_0^f), which are commonly measured material properties. After a survey of materials, a large $\eta \sim 80\%$ is predicted to be achievable in a (001)-oriented tetragonal $(K_{0.5}, Na_{0.5})NbO_3$ film. This strain-stabilized tetragonal phase is verified by density functional theory (DFT) calculations. $(K_{0.5}, Na_{0.5})NbO_3$ films based on this design were successfully prepared via a sputtering deposition process on $SrRuO_3$ -buffered (100) $SrTiO_3$ substrates. The resulted epitaxial films showed a sizable P_0^f ($\sim 0.21 C m^{-2}$) and a large χ_0^f (~ 830 – 860), as well as a large η close to the theoretical value. The measured dielectric tunabilities as functions of E are well described by the theoretical $\eta(E)$ curves, validating our integrated approach rooted in a theoretical understanding.

npj Computational Materials (2021)7:62; <https://doi.org/10.1038/s41524-021-00528-2>

INTRODUCTION

Tunable dielectrics is a type of functional materials whose dielectric permittivity (χ) can be adjusted by an external electric field E . The key parameter used to describe a tunable dielectric is the so-called dielectric tunability, η , which is defined as the relative change (%) of dielectric permittivity under an E field: $\eta(E) = \frac{\chi_0 - \chi(E)}{\chi_0} \times 100\%$. Here χ_0 is the zero-field or small-field dielectric permittivity while $\chi(E)$ is the one under the field E . As a typical nonlinear dielectric, ferroelectrics are usually endowed with a high dielectric tunability, and hence have been broadly utilized in tunable dielectric devices. Recently, with the rapid developments in miniaturized and integrated tunable devices, such as phase shifters, oscillators, and filters, ferroelectric thin films showing a high η value have been extensively investigated^{1–3}. PZT and some lead-free films including $BaTiO_3$ ^{4–6}, $(Ba, Sr)TiO_3$ ^{1,7–9}, and $Ba(Zr, Ti)O_3$ ¹⁰ are the center of focus based on their high dielectric permittivities. The reported η values are usually between 20 and 70%^{1,6,7,11,12}.

Currently, there are a few issues that need to be addressed for the further development of tunable ferroelectric dielectrics. Firstly, $BaTiO_3$ -based ferroelectrics have a relatively low Curie temperature ($< \sim 120^\circ C$) which has limited their applications, while the use of lead-based ferroelectrics (such as PZT) at elevated temperatures exacerbates the risk of toxic lead exposure. Secondly, the measured η values^{13–19} are usually not quantitatively explained, except for a few cases in bulk ceramics^{20,21}. This is possibly due to the many practical factors affecting dielectric tunability in thin films, as well as disconnects between theorists and experimentalists. In this work, a coordinated effort integrating computational material design, material processing, and electrical characterization is reported for (001)-oriented epitaxial $(K_{0.5}, Na_{0.5})NbO_3$ (KNN) films. As will be illustrated below, KNN in this structure is a promising material candidate for thin-film tunable dielectrics,

owing to its lead-free composition, high Curie temperature, a sizable spontaneous polarization, and a large dielectric permittivity^{22–25}.

RESULTS AND DISCUSSION

Dielectric tunability of a (001)-oriented tetragonal ferroelectric film

For a (001)-oriented tetragonal ferroelectric film of an epitaxial quality, its polarization P is aligned along the film normal under an external electric field E , the in-plane polarization, and electrical field components $P_1 = P_2 = 0, E_1 = E_2 = 0$, while the out-of-plane ones are not, $P_3 = P \neq 0, E_3 = E$. The in-plane strains extrapolated to the parent cubic phase, are $\epsilon_1 = \epsilon_2 = u_m = \epsilon_M^0 + Q_{12}(P_0^b)^2$ ²⁶, where ϵ_M^0 is the effective in-plane misfit, i.e., the difference between in-plane lattice parameters of the clamped and free-standing films, Q_{12} is an electrostrictive coefficient, and P_0^b is the spontaneous polarization of the free-standing film or bulk. The Landau-Devonshire type (LD) thermodynamic potential of the film can be expressed as²⁶:

$$\tilde{G} = a_1 P^2 + a_{11} P^4 + a_{111} P^6 - EP + \frac{\left\{ \epsilon_M^0 - Q_{12} \left[P^2 - (P_0^b)^2 \right] \right\}^2}{S} \quad (1)$$

where a_1, a_{11}, a_{111} are the first, second, and third-order Landau coefficients determined under the stress-free condition, and S is the effective in-plane compliance given by $S = s_{11} + s_{12}$, with s_{11}, s_{12} being the elastic compliances of the parent cubic phase. These material-specific parameters can be obtained from experimental measurements. By using the combo coefficients below²⁶,

$$\alpha = 2 \left(a_1 - \frac{2[\epsilon_M^0 + Q_{12}(P_0^b)^2]Q_{12}}{S} \right), \beta = 4 \left(a_{11} + \frac{Q_{12}^2}{S} \right), a_3 = 6a_{111} \quad (2)$$

¹Key Laboratory for Liquid-Solid Structure Evolution and Processing of Materials (Ministry of Education), School of Materials Science and Engineering, Shandong University, Jinan, China. ²Institute of Advanced Energy Materials and Chemistry, Shandong Provincial Key Laboratory of Molecular Engineering, School of Chemistry and Chemical Engineering, Qilu University of Technology (Shandong Academy of Sciences), Jinan, China. ³International Centre for Quantum and Molecular Structures, Department of Physics, Shanghai University, Shanghai, China. ⁴School of Materials Science and Engineering, University of Jinan, Jinan, China. ✉email: liyang@shu.edu.cn; mse_huany@ujn.edu.cn; ouyangjun@qlu.edu.cn

We reduce Eq. (1) into

$$\tilde{G} = \frac{1}{2}aP^2 + \frac{1}{4}\beta P^4 + \frac{1}{6}a_3P^6 - EP + \frac{[\epsilon_M^0 + Q_{12}(P_0^b)^2]^2}{S} \quad (3)$$

The equilibrium polarization under an electric field E can be obtained by minimizing the free energy in Eq. (3), i.e., $d\tilde{G}/dP = 0$, which leads to

$$E = \alpha P + \beta P^3 + a_3 P^5 \quad (4)$$

when $E = 0$, the film's remnant polarization can be obtained,

$P_0^f = \sqrt{\frac{-\beta + (\beta^2 - 4a\alpha_3)^{1/2}}{2a_3}}$. Using a field-induced polarization $p = P^f(E) - P_0^f$, the zero-field dielectric permittivity of the film (χ_0^f) can also be obtained from an approximation of Eq. (4), taking into account only the first term,

$$E = [a + 3\beta(P_0^f)^2 + 5a_3(P_0^f)^4]p \quad (5)$$

$$\chi_0^f = \frac{dp}{dE}|_{E=0} = [a + 3\beta(P_0^f)^2 + 5a_3(P_0^f)^4]^{-1} \quad (6)$$

If the second-order term is taken into account, Eq. (4) reduces to

$$E = \gamma_1 p + \gamma_2 p^2 \quad (7)$$

where $\gamma_1 = (\chi_0^f)^{-1}$, $\gamma_2 = 3\beta P_0^f + 10a_3(P_0^f)^3$.

From the solution of Eq. (7) we can obtain the dielectric permittivity under an applied electric field E ,

$$\chi^f(E) = \frac{dp}{dE} = \frac{1}{\sqrt{\gamma_1^2 + 4\gamma_2 E}} = \frac{\chi_0^f}{\sqrt{1 + \lambda_f E}} \quad (8)$$

$$\text{where } \lambda_f = \frac{4\gamma_2}{\gamma_1^2} = 4(\chi_0^f)^2 \cdot [3\beta P_0^f + 10(P_0^f)^3 a_3] \quad (9)$$

It is noted that Eq. (8) reveals the nonlinear nature of the dielectric permittivity in a ferroelectric film. λ_f is the tunability factor of the ferroelectric film, which characterizes the rate of the nonlinear change of its dielectric permittivity. Consequently, the dielectric tunability η can be expressed as:

$$\eta = \frac{\chi_0^f - \chi^f(E)}{\chi_0^f} \times 100\% = 1 - \frac{1}{\sqrt{1 + \lambda_f E}} \quad (10)$$

From Eq. (10), it is clear that the dielectric tunability η has a positive correlation with λ_f . The larger the λ_f , the higher the reduced portion of χ_0^f , i.e., the higher the dielectric tunability η is, at a given electric field E . From Eq. (9), λ_f and hence η is determined by the directly measurable material properties χ_0^f and P_0^f , given that the material-specific parameters of a_{11} , a_{111} , S and Q_{12} are known (In principle, all three parameters λ_f , χ_0^f and P_0^f are functions of the misfit strain ϵ_M^0 . They can be determined theoretically when the Landau coefficients (a_1 , a_{11} , a_{111}), the electrical/elastic/electromechanical properties (P_0^b , s_{11}/s_{12} and Q_{12}) of the film material, as well as its misfit strain ϵ_M^0 are all correctly determined. However, this is not always possible for theorists or convenient for experimentalists. In this work, for the selection of material, we used the experimentally measurable properties of χ_0^f and P_0^f , which are abundant in the literature, and a reduced number of material-specific parameters).

In Fig. 1 below, the tunability factors λ_f for some commonly used, (001)-oriented tetragonal ferroelectric films are presented as functions of χ_0^f and P_0^f . It clearly shows that, with an intermediate remnant polarization ($P_0^f \sim 0.15$ to 0.3), a large dielectric permittivity (second only to PZT 50/50 in this chart, $\chi_0^f \sim 600$ – 1200 ^{18,25,27,28}), (001)-oriented tetragonal KNN films display a large λ_f on the order of 10^{-6} – 10^{-7} , corresponding to a dielectric tunability $\eta \sim 59$ – 86% under a typical electric field of 500 kV cm^{-1} (5 V on a 100 nm thick film). This is very promising for a lead-free ferroelectric.

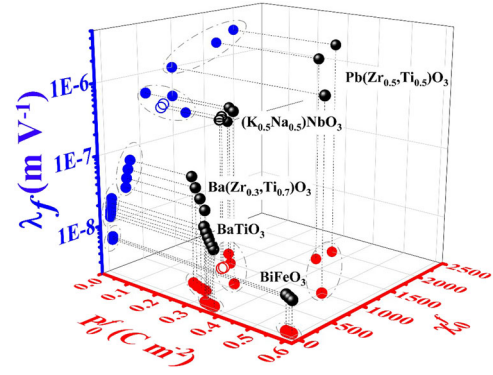


Fig. 1 Relationship between λ_f , χ_0^f and P_0^f . The relationship between λ_f , χ_0^f and P_0^f of typical (001)-oriented tetragonal ferroelectric films, including BaTiO₃, Ba(Zr_{0.3}Ti_{0.7})O₃, BiFeO₃, K_{0.5}Na_{0.5}NbO₃, and Pb(Zr_{0.5}Ti_{0.5})O₃. The two open-circle points are experimental data from this work. The ellipses are drawn for the guidance of the eye.

Table 1. Parameters used for BTO, BZT 30/70, BFO, PZT 50/50 films in Fig. 1.

Parameters	Units	BTO	BZT30/70	BFO	PZT50/50
a_{11} (10^8)	$\text{C}^{-4}\text{m}^6\text{N}$	-6.48	8.9	6.5	0.4764
a_{111} (10^9)	$\text{C}^{-6}\text{m}^{10}\text{N}$	8	-2.11	0.006	0.1336
s_{11} (10^{-12})	m^2N^{-1}	8.01	6.839	4.25	10.5
s_{12} (10^{-12})	m^2N^{-1}	-1.66	-2.093	-4	-3.7
Q_{12}	C^2m^4	-0.045	-0.0355	-0.016	-0.046
β (10^9)	$\text{C}^{-4}\text{m}^6\text{N}$	-1.32	4.26	7.94	1.44
a_3 (10^7)	$\text{C}^{-6}\text{m}^{10}\text{N}$	4802	-1260	3.6	80.2
References		29	30	31–33	34

The Landau coefficients and other related parameters of the ferroelectric films in Fig. 1 are listed in Tables 1 and 2, for BaTiO₃ (BTO)²⁹, Ba(Zr_{0.3}Ti_{0.7})O₃ (BZT 30/70)³⁰, BiFeO₃ (BFO)^{31–33} and Pb(Zr_{0.5}Ti_{0.5})O₃ (PZT 50/50)³⁴ films, and (K_{0.5}Na_{0.5})NbO₃ (KNN) films³⁵, respectively.

Strain-stabilized (001)-oriented tetragonal KNN film

A modified-LD thermodynamic potential has been employed to predict the crystalline structure of an epitaxial KNN film³⁵. The thermodynamic potential \tilde{G} of a single-domain epitaxial film under a constant-stress mechanical boundary condition can be written as^{36–40}:

$$\begin{aligned} \tilde{G} = & a_1(P_1^2 + P_2^2 + P_3^2) + a_{11}(P_1^4 + P_2^4 + P_3^4) + a_{111}(P_1^6 + P_2^6 + P_3^6) \\ & + a_{12}(P_1^2 P_2^2 + P_1^2 P_3^2 + P_2^2 P_3^2) + a_{123} P_1^2 P_2^2 P_3^2 \\ & + a_{112}[P_1^4(P_2^2 + P_3^2) + P_2^4(P_1^2 + P_3^2) + P_3^4(P_1^2 + P_2^2)] \\ & - \frac{1}{2}s_{11}(\sigma_1^2 + \sigma_2^2 + \sigma_3^2) - s_{12}(\sigma_1\sigma_2 + \sigma_1\sigma_3 + \sigma_2\sigma_3) \\ & - \frac{1}{2}s_{44}(\sigma_4^2 + \sigma_5^2 + \sigma_6^2) - Q_{11}(\sigma_1 P_1^2 + \sigma_2 P_2^2 + \sigma_3 P_3^2) \\ & - Q_{12}[\sigma_1(P_2^2 + P_3^2) + \sigma_2(P_1^2 + P_3^2) + \sigma_3(P_1^2 + P_2^2)] \\ & - Q_{44}(\sigma_4 P_2 P_3 + \sigma_5 P_1 P_3 + \sigma_6 P_1 P_2) - (P_1 E_1 + P_2 E_2 + P_3 E_3) \end{aligned} \quad (11)$$

where a_1 , a_{11} , a_{12} , a_{111} , a_{112} and a_{123} are the first and high-order Landau coefficients determined under the stress-free condition. P_i ($i = 1-3$) and σ_j ($j = 1-6$) are the i th polarization and j th stress components, respectively. s_{11} , s_{12} , and s_{44} are the elastic compliances of the parent cubic phase, while Q_{11} , Q_{12} , and Q_{44} are the electrostrictive coefficients.

Table 2. Parameters of KNN films used in theoretical computations of this work³⁵.

Parameters	Values	Units	Coeff.	Values	Units
a_1	-1.6042×10^8	$C^{-2}m^2N$	s_{11}	5.6×10^{-12}	m^2N^{-1}
a_{11}	-2.7302×10^8	$C^{-4}m^6N$	s_{12}	-1.6×10^{-12}	m^2N^{-1}
a_{111}	3.0448×10^9	$C^{-6}m^{10}N$	s_{44}	-1.3×10^{-12}	m^2N^{-1}
a_{12}	1.0861×10^9	C^4m^6N	p_0^f	0.21	Cm^{-2}
a_{112}	-2.727×10^9	$C^6m^{10}N$	ϵ_M^0	-0.018	N/A
a_{123}	1.5513×10^{10}	$C^6m^{10}N$	β	-4.1608×10^8	$C^{-4}m^6N$
Q_{11}	0.16	C^2m^4	α_3	1.82688×10^{10}	$C^{-6}m^{10}N$
Q_{12}	-0.026	C^2m^4	$\lambda_f(150 \text{ nm})$	2.85×10^{-7}	mV^{-1}

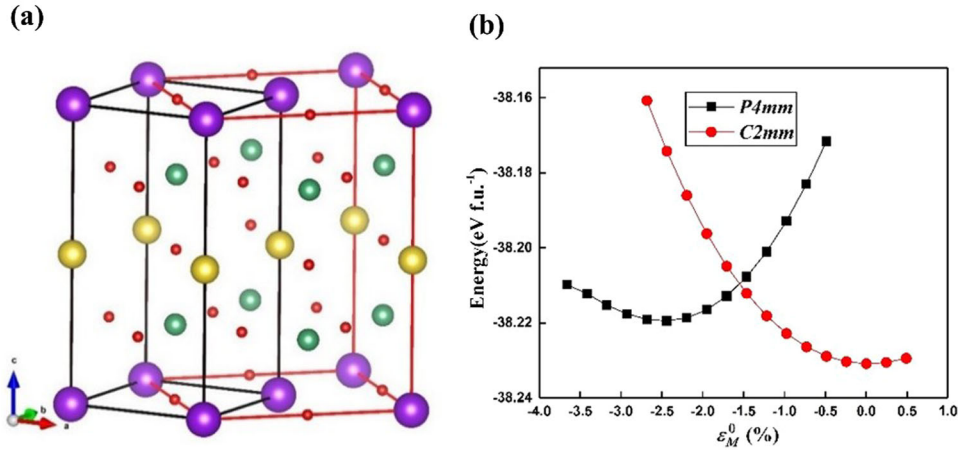


Fig. 2 Relevant results of DFT theoretical calculation. **a** Schematic diagram of ideal paraelectric KNN structure. The atoms are ordered along [001] direction. The atoms in yellow, purple, green, and red are K, Na, Nb, and O, respectively. The unit cell in black frame and the supercell in red frame contains 10 and 20 atoms, respectively, and will be used in our calculation for different KNN phases, i.e., $P4mm$ (10 atoms) and $C2mm$ (20 atoms). **b** Free energies of the $P4mm$ and $C2mm$ phases as functions of the misfit strain.

For an epitaxial oxide film, its in-plane strains decrease slowly with film thickness, after its initial relaxation via the formation of misfit dislocations in the first ~ 10 – 50 nm thick layer^{41,42}. Therefore, for a few hundred nm thick or thicker oxide film, its in-plane strains are residual ones post relaxation, and can be considered as fixed/thickness-independent. Moreover, the stress components σ_3 , σ_4 , and σ_5 are zero because of the film's free surface. The relationship between the other in-plane strains ϵ_i ($i = 1, 2, 6$) and stress components can be obtained from the thermodynamic relations: $\frac{\partial \tilde{G}}{\partial \sigma_1} = -\epsilon_1$, $\frac{\partial \tilde{G}}{\partial \sigma_2} = -\epsilon_2$, $\frac{\partial \tilde{G}}{\partial \sigma_6} = -\epsilon_6$.

For a (001) ferroelectric thin film epitaxially grown in its cubic paraelectric phase on a (100)-oriented cubic substrate, the in-plane strains are $\epsilon_1 = \epsilon_2 = u_m = \epsilon_M^0 + Q_{12}(P_0^0)^2$ and $\epsilon_6 = 0$. So, the thermodynamic potential becomes³⁷:

$$\begin{aligned} \tilde{G} = & a_1^f(P_1^2 + P_2^2) + a_3^f P_3^2 + a_{11}^f(P_1^4 + P_2^4) + a_{33}^f P_3^4 + a_{13}^f(P_1^2 P_3^2 + P_2^2 P_3^2) \\ & + a_{12}^f P_1^2 P_2^2 + a_{111}^f(P_1^6 + P_2^6 + P_3^6) + a_{112}^f[(P_1^2 + P_2^2)P_1^4 + (P_1^2 + P_2^2)P_2^4 + (P_1^2 + P_2^2)P_3^4] \\ & + a_{123}^f P_1^2 P_2^2 P_3^2 + \frac{u_m^2}{s_{11} + s_{12}} - (P_1 E_1 + P_2 E_2 + P_3 E_3) \end{aligned} \quad (12)$$

where $a_1^f = a_1 - \frac{(Q_{11} + Q_{12})u_m}{s_{11} + s_{12}}$, $a_3^f = a_3 - \frac{Q_{12}u_m}{s_{11} + s_{12}}$, $a_{11}^f = a_{11} + \frac{s_{11}(Q_{11}^2 + Q_{12}^2) - 2Q_{11}Q_{12}s_{12}}{2(s_{11}^2 - s_{12}^2)}$, $a_{12}^f = a_{12} - \frac{s_{12}(Q_{11}^2 + Q_{12}^2) - 2Q_{11}Q_{12}s_{11}}{s_{11}^2 - s_{12}^2} + \frac{Q_{44}^2}{2s_{44}}$, $a_{13}^f = a_{12} + \frac{(Q_{11} + Q_{12})Q_{12}}{s_{11} + s_{12}}$, $a_{33}^f = a_{11} + \frac{Q_{12}^2}{s_{11} + s_{12}}$, a_{11}^f , a_{33}^f , a_{11}^f , a_{12}^f , a_{13}^f and a_{33}^f are the modified Landau coefficients of the film. The equilibrium thermodynamic states can be determined via minimization of \tilde{G} ($\frac{\partial \tilde{G}}{\partial P_1} = 0$, $\frac{\partial \tilde{G}}{\partial P_2} = 0$, $\frac{\partial \tilde{G}}{\partial P_3} = 0$). For a KNN film, all the parameters used in the calculations are listed in Table 2. The KNN film is in a

tetragonal phase at room temperature ($P_1 = P_2 = 0$, $P_3 = P \neq 0$) when ϵ_M^0 is between -1.0 and -2.0% . This result is consistent with the theoretical works reported in the literature^{35,37}. For undoped $(K_{0.5}Na_{0.5})NbO_3$ films grown on a commonly used perovskite-type semiconductor substrate ($SrTiO_3$, $LaAlO_3$, $(La,Sr)(Al,Ta)O_3$, etc.), this strain condition is readily achievable.

On the experimental side, there are several groups reporting strain- or composition-induced phases in $(K_xNa_{1-x})NbO_3$ -based epitaxial films^{43–46}. For example, Luo et al. revealed a strain-induced monoclinic phase in Li⁴³ and Mn-doped⁴⁴ KNN films, which shows an enhance piezoelectric response. Helden et al.⁴⁵ revealed a linear correlation between the phase transition temperature from a strain-stabilized monoclinic phase to the orthorhombic c-phase in $(K_xNa_{1-x})NbO_3$ films ($x = 0.54$ – 0.77), and the applied overall lattice strain from the sum of the anisotropic in-plane compressive misfit strains with the substrate. Shiraishi et al.⁴⁶ showed a systematic reduction of the orthorhombic–tetragonal and tetragonal–cubic phase transition temperatures by increasing the Ta-dopant amount in thick epitaxial $(K,Na)(Nb,Ta)O_3$ films deposited by using the hydrothermal method. Together, these works provided the foundation for engineering the phase structures in KNN films.

It is noted that, unlike those of well-studied ferroelectrics, such as PZT or $BaTiO_3$, the material parameters of KNN in its LD potential are not all determined from experimental measurements³⁵. To verify this material design, we used density functional theory (DFT) calculations^{47–49} to investigate the relative stability between the bulk orthorhombic and the strain-induced tetragonal phases.

As shown in Fig. 2a, the supercells with K and Na atoms orderly distributed along the [001] direction are adopted in our

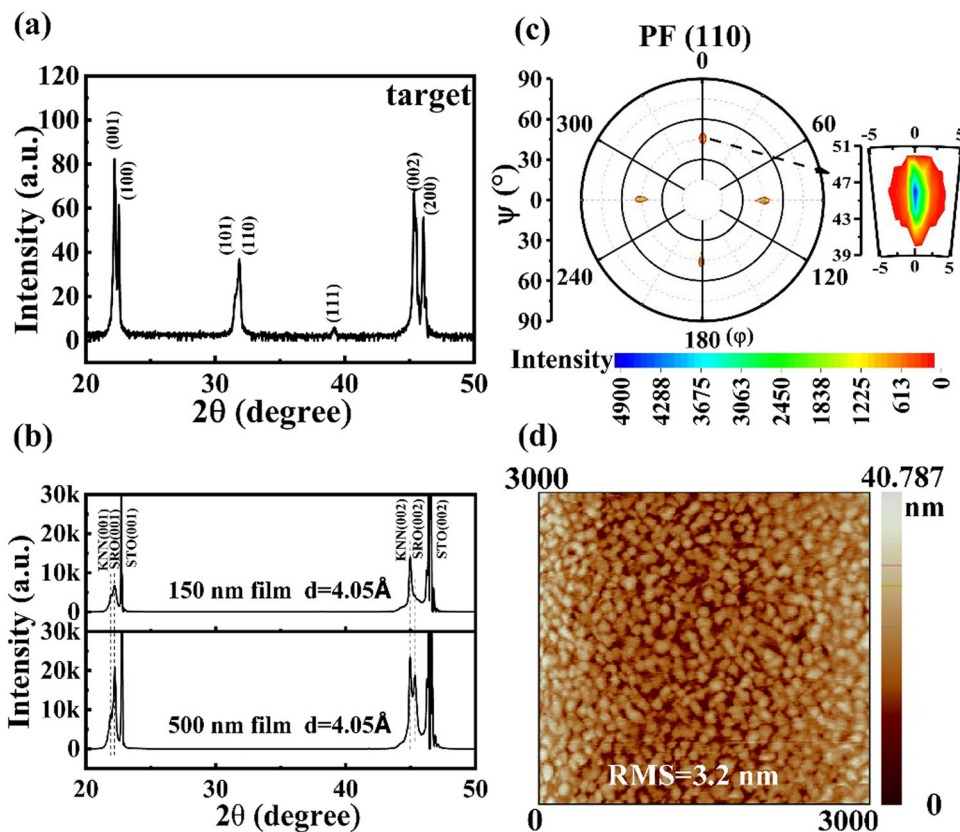


Fig. 3 Microstructure and morphology of KNN target and films. X-ray diffraction 2θ scan patterns of (a) the KNN ceramic target and (b) 150 nm- and 500 nm-thick KNN films; c the (110) XRD pole figure of the 500 nm KNN film; d an AFM surface scan image of the 150 nm KNN film.

simulation. Moreover, two different phases, i.e., tetragonal $P4mm$ and orthorhombic $C2mm$ which contain 10 and 20 atoms, respectively, are considered for their relative stabilities under a biaxial strain. The misfit strain of the KNN structure can be represented by: $\varepsilon_M^0(\%) = \frac{a-a_0}{a_0} \times 100\%$, where a_0 is the in-plane lattice parameter of the bulk stable phase of $C2mm$. The free energy-misfit strain diagram for the two phases is shown in Fig. 2b. It clearly shows that a compressive strain will destabilize the bulk $C2mm$ phase, and induce the tetragonal $P4mm$ phase. The transition point is at $\varepsilon_M^0 \sim -1.5\%$, fairly consistent with the prediction based on the LD thermodynamic computation^{35,37}.

Analysis of microstructure and chemical states of the KNN films

Based on the above analysis, we designed and obtained (001)-oriented tetragonal KNN films (150 and 500 nm thick) via RF magnetron sputtering on SrRuO₃ (SRO)-buffered (100) SrTiO₃ (STO) substrates, which showed a high tunability factor $\lambda_f \sim 3 \times 10^{-7}$, and a large dielectric tunability $\sim 80\%$.

Figure 3 shows the microstructural characteristics of the KNN target and films. In Fig. 3a, except for the XRD peaks corresponding to a bulk orthorhombic phase of KNN50/50⁵⁰, no other secondary phases were detected in the KNN ceramic target. The lattice parameters of the target are $c_{pc} = a_{pc} = 3.997 \text{ \AA}$, $b_{pc} = 3.938 \text{ \AA}$, respectively. In Fig. 3b, both KNN films show a (001)-orientation with an out-of-plane lattice parameter of $\sim 4.05 \text{ \AA}$. Furthermore, in the (110) pole figure (Fig. 3c), the diffracted X-ray signals display a fourfold symmetry at a tilt angle of $\sim 45^\circ$, indicating a heteroepitaxial growth of the KNN film with a (001) out-of-plane orientation⁵¹. It will be revealed later, that these films have a tetragonal symmetry with a (001)-orientation promoted by

the SRO buffer layer, which lowered the surface energy of the (001) crystalline plane. The 4.05 \AA out-of-plane lattice parameter corresponds to an in-plane compressive strain of $\sim -1.8\%$ ($\varepsilon_{xx} = \varepsilon_{yy} = -\frac{1-\nu}{2\nu} \varepsilon_{zz}$, ε_{zz} is the out-of-plane strain, $\varepsilon_{zz} = \frac{c_{\text{film}} - c_{\text{bulk}}}{c_{\text{bulk}}}$, c_{film} and c_{bulk} are the out-of-plane lattice parameters of the KNN film and bulk ceramic, ν is the Poisson's ratio, which is ~ 0.27 for KNN⁵²). This compressive strain is responsible for the elongation of the out-of-plane lattice parameter and shortening of the in-plane a and b lattice parameters. Lastly, a representative AFM surface scan image of the 150 nm KNN film is shown in Fig. 3d. The film is dense and uniform, displaying a smooth surface with a root-mean-square (RMS) roughness of $\sim 3.2 \text{ nm}$.

Figure 4a and e are representative cross-sectional bright-field TEM images of the 150 nm and 500 nm KNN film, respectively, which reveal clean and sharp interfaces in the KNN/SRO/STO heterostructure. The thicknesses of the SRO layer in both films were $\sim 60 \text{ nm}$. In the high-resolution TEM images shown in Fig. 4b, c, f, and g, atomically coherent interfaces (marked by dashed white lines) between the (100) STO substrate and the SRO layer, SRO and KNN layers were revealed, validating a (001) heteroepitaxial growth in the two films. Figure 4d is a selected area electron diffraction (SAED) pattern of the boxed region in Fig. 4c via a fast-Fourier transformation (FFT), while Fig. 4h is a SAED pattern directly taken from the circled region in Fig. 4e. The zone axis is [010] for both SAED patterns. The measured out-of-plane and in-plane lattice parameters of the KNN films were $\sim 4.05 \text{ \AA}$ and $\sim 3.93 \text{ \AA}$, respectively. The sharp electron diffraction spots in Fig. 4d and h indicate that the films are of epitaxial quality, consistent with the XRD results displayed in Fig. 3.

Surface XPS spectra of the 150 nm KNN film were collected to analyze the valence states of the elements. The core-level

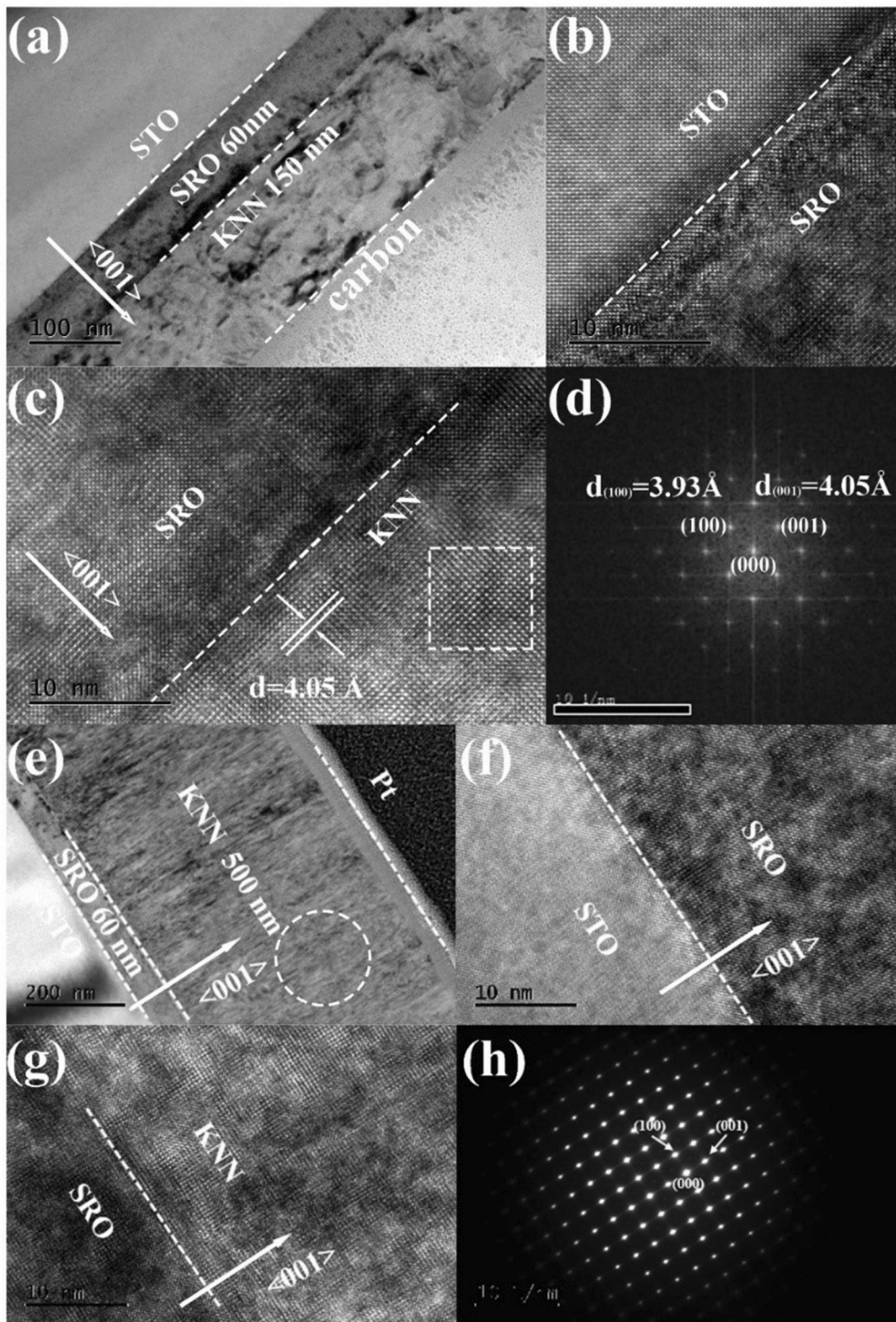


Fig. 4 Cross-sectional microstructure of KNN films. Cross-sectional bright-field TEM images of the KNN/SRO/STO heterostructure with the KNN thickness of (a) 150 nm and (e) 500 nm; b–c and f–g are the high-resolution TEM images near the SRO/STO and KNN/SRO interfaces for the 150 nm and 500 nm thick KNN films, respectively; d and h are the selected area electron diffraction patterns of the boxed and circled regions in (c) and (e), respectively.

elemental binding energies were all calibrated by using the carbon 1s peak (284.8 eV), and the XPS spectra were fitted by using the Avantage software. Figure 5a is the survey spectrum which showed clear signals from K, Na, Nb, and O, as well as a trace amount of the environment C. No fingerprints of any other element were found in the survey spectrum, which proved the chemical purity of the KNN film. Figure 5b is the core level K 2p

XPS spectrum. The K 2p XPS peak from the K element in the KNN lattice splits into doublets (K 2p_{3/2} and K 2p_{1/2})^{53–57}. There is a very weak second group of doublets, marked as K 2p'_{3/2} and K 2p'_{1/2}, which can be attributed to a small amount of K existing in the form of K₂O^{53–57}. The existence of potassium oxide on the film surface is usually unavoidable^{53–57}, which can be attributed to the effects of composition variation and different evaporation rates of

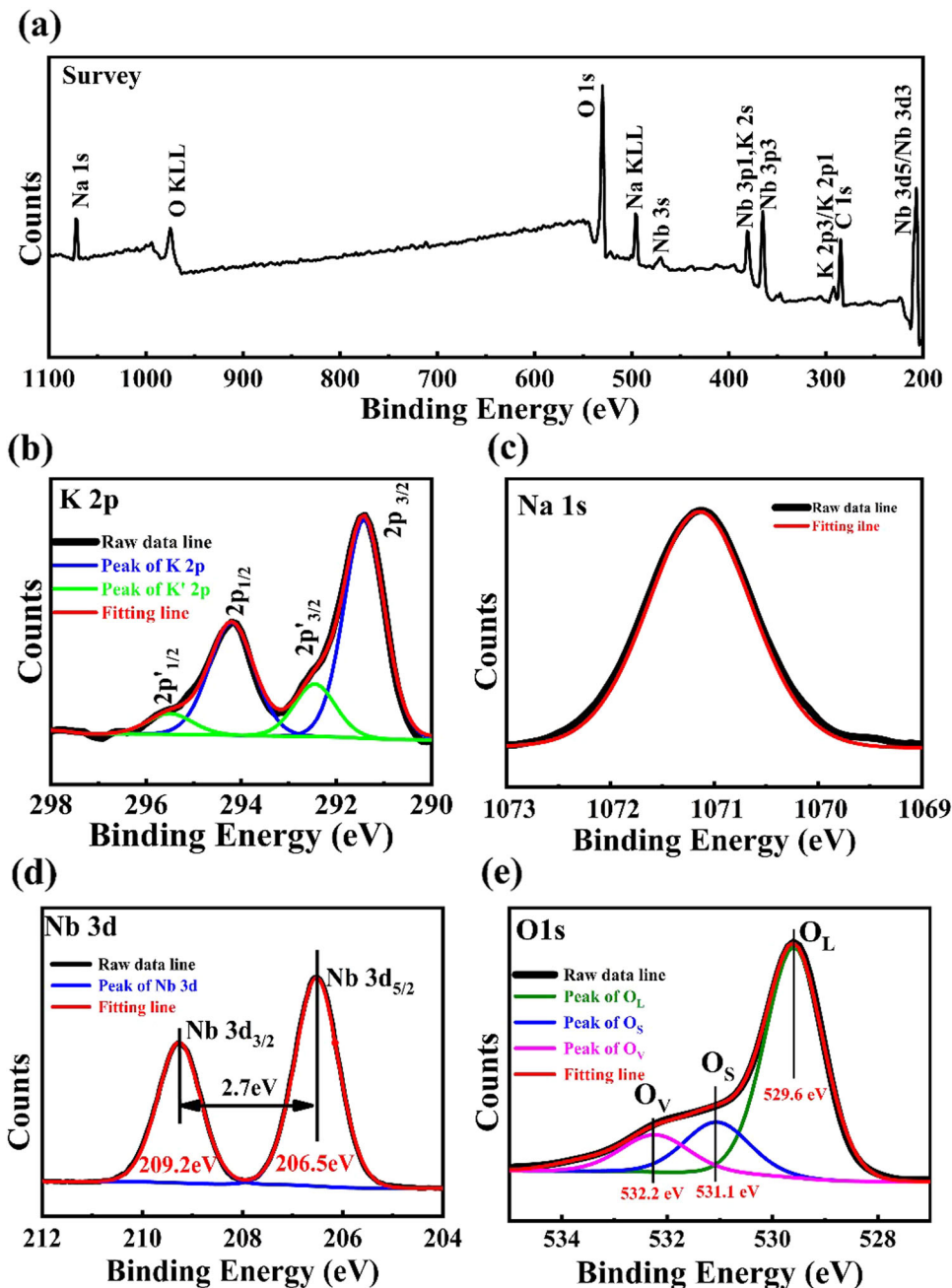


Fig. 5 Chemical properties of the KNN films. **a** survey spectrum and **(b–e)** narrow-scan spectra of **(b)** K 2p, **(c)** Na 1s, **(d)** Nb 3d, and **(e)** O 1s core levels from the 150 nm KNN film.

the component species in the KNN target and film. Furthermore, the 1s core-level XPS spectrum of Na and the 3d core-level XPS spectrum of Nb are shown in Fig. 5c and d, respectively. The Na 1s peak is symmetrical and shows no split or shift of peak position. It is well fitted to the standard peak for the sodium element in the KNN lattice. On the other hand, the Nb peak splits into doubles ($3d_{3/2}$ and $3d_{5/2}$) with a binding energy difference of ~ 2.7 eV, confirming the existence of Nb–O bonds and a Nb^{5+} valence state in the film⁵⁸. Figure 5e is the O 1s core-level XPS spectrum, which is asymmetric and can be decomposed into three characteristic peaks, indicating the existence of three oxygen species on the film surface. The peak located at the low energy side (529.6 eV) is associated with the lattice oxygen (O_L). The middle peak, located at 531.1 eV, corresponds to adsorbed oxygen on the surface (O_S), which may have a variety of states, such as O^- , O_2^{2-} , etc. Lastly,

the peak located at 532.2 eV is associated with oxygen vacancies (O_V)⁵⁹. The formation of oxygen vacancies on the surface of a KNN film is commonly observed^{60,61}, which can be attributed to the evaporation loss of volatile alkali ions⁵⁵.

Electrical performance

Figure 6a shows the measured P – E hysteresis loops of the two KNN films (@1 kHz). Both films display a remnant polarization of $\sim 21 \mu\text{C cm}^{-2}$. In Fig. 6b, the measured dielectric permittivity χ –electric field E (χ – E) curve of the 500 nm film is well fitted by the theoretical results given by Eqs. (8) and (9), while that of the 150 nm film was offset from the computed χ – E curve by a small field/voltage (~ 0.225 V, inset of Fig. 6b). This small offset can be attributed to a non-negligible voltage drop across an interface

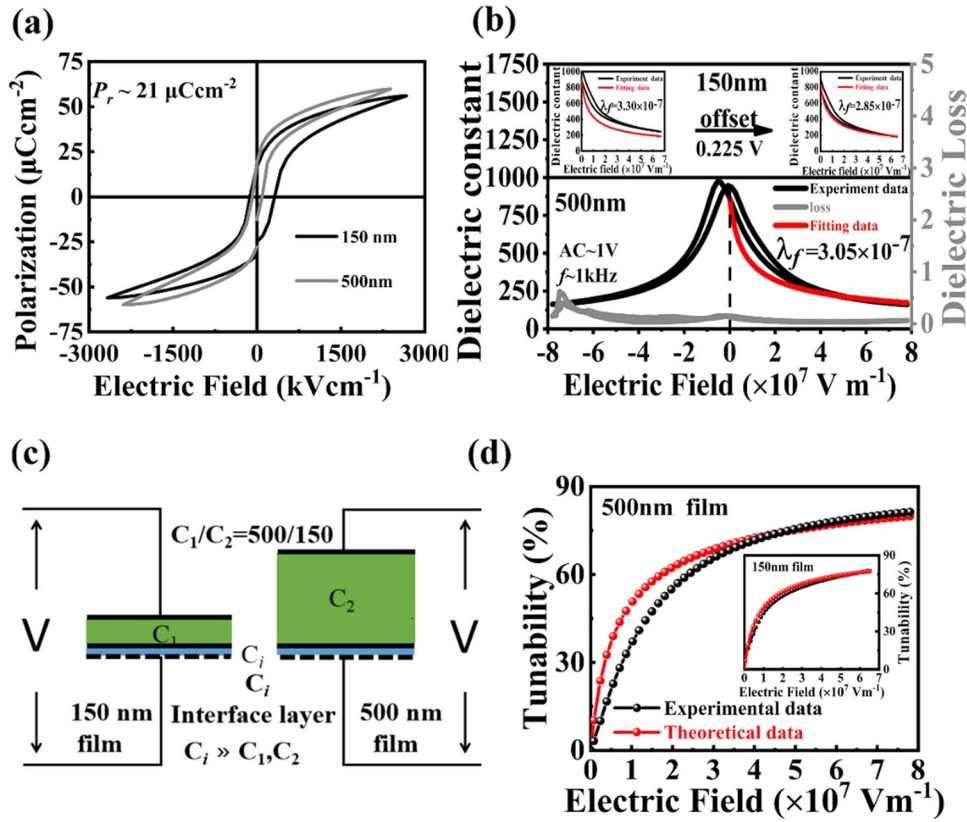


Fig. 6 Electrical performance of the KNN films. **a** Polarization-electric field (P - E) hysteresis loops (measured @1 kHz); **b** measured and computed dielectric permittivity χ -electric field E (χ - E) curves of the 500nm-thick KNN film ($\lambda_f = 3.05 \times 10^{-7} \text{ m V}^{-1}$ from Eq. 9), the inset shows the measured and computed χ - E curves ($E > 0$) of the 150nm-thick film under 10V ($\lambda_f = 2.85 \times 10^{-7} \text{ m V}^{-1}$ from Eq. 9). The dielectric loss tangent-electric field ($\text{tg}\delta$ - E) curves are also shown for the 500 nm film. **c** Schematic illustration of the effect of a capacitive interface layer on reducing the effective voltage across the KNN film. The thinner the KNN film, the larger the voltage drop on this interface layer. **d** Measured (@1 kHz) and computed dielectric tunabilities as functions of the bias field for the 500 and 150 nm (inset) KNN films.

capacitive layer. The effect of such an interface layer is schematically shown in Fig. 6c. A simple model of serially connected capacitors is used to illustrate the effect of film thickness on the voltage drop across a thin interface layer⁶². When the KNN film is thick enough, its capacitance becomes very low compared with that of the interface layer, and hence nearly 100% of the applied voltage drops across the KNN film. The interfacial voltage drop only becomes non-negligible when the film is much thinner (500 nm \rightarrow 150 nm). After correction of this small offset, it is noted that there is only a small difference between the computed tunability factors λ_f (via Eq. (9)) of the two films, $3.05 \times 10^{-7} \text{ m V}^{-1}$ for the 500 nm film and $2.85 \times 10^{-7} \text{ m V}^{-1}$ for the 150 nm one, which can be attributed to their slightly different remnant dielectric permittivities ($\chi_0^r \sim 860$ and ~ 830 for the 500 nm and 150 nm KNN films, respectively). In addition, the dielectric loss tangent-electric field ($\text{tg}\delta$ - E) curve is also shown for the 500 nm film. The losses are in a reasonable range (~ 0.03 to ~ 0.1) except at the high negative bias end. This is possibly due to the asymmetric electrode interfaces⁶². Lastly, Fig. 6d displays the experimental and computed dielectric tunability-electric field (η - E) curves for the two KNN films. The experimental curves were derived from the χ - E data in Fig. 6b, while the theoretical curves were computed by using Eqs. (9) and (10), with a 0.225 V voltage offset correction performed for the 150 nm film. The experimental and theoretical dielectric tunabilities agreed fairly well with each other, especially in the high electric field end, where both curves saturate with an increasing field. The small gap between the experimental tunability and the theoretical one, which exists in

the low-to-middle field range, can be attributed to charged defects in the films, which demand an extra amount of energy to be aligned with the applied electric field. Effects of these extrinsic charges diminish under a high electric field, hence the measured tunabilities (and dielectric permittivities as shown in Fig. 6b) behaved just like the theory predicted in the high field end. Number-wise, the designed high tunability values have been achieved in the KNN films. For the 150 nm-thick KNN film, the theoretical tunability η under an electric field of $6.5 \times 10^7 \text{ (V m}^{-1}\text{)}$ (10 V) is 77.4%, while the measured η is 77.7%. For the 500 nm-thick KNN film, the computed and measured η values at $7.8 \times 10^7 \text{ (V m}^{-1}\text{)}$ (39 V) were 80% and 81%, respectively. These numbers are the highest reported η values so far for KNN thin film dielectrics^{17-19,25,63}.

In this work, (001)-oriented, strain-stabilized tetragonal KNN thin films with a high dielectric tunability were successfully designed via computational approaches using the LD type thermodynamic potential and DFT calculations. These KNN films were epitaxially grown on SrRuO₃-buffered (100) SrTiO₃ substrates via RF magnetron sputtering. A high remnant polarization P_0^r ($\sim 21 \mu\text{C cm}^{-2}$) and a large small-field dielectric permittivity χ_0^r (~ 830 – 860) were achieved in these films. The measured maximum dielectric tunabilities η (~ 75 – 80%) are in good agreement with the computed theoretical values. Moreover, their field dependences, i.e., the η - E curves, can be well described by our equation derived using the LD theory. These results suggest that, the dielectric tunability of a ferroelectric film, as its key performance parameter in tunable dielectrics, can be predicted using a computational approach.

METHODS

DFT calculations

The DFT calculations were performed with the projector augmented wave (PAW) approach⁴⁷, as implemented in the Vienna ab initio simulation package (VASP)⁴⁸. The electron exchange-correlation functional was treated by generalized gradient approximation (GGA) in the form of Perdew–Burke–Ernzerhof (PBE)⁴⁹. The plane-wave cutoff and convergence criteria for energy and force are set to be 550 eV, 10^{-7} eV, and $0.01 \text{ eV}\text{\AA}^{-1}$, respectively.

Sintering of the KNN ceramic target

The KNN 50/50 ceramic target was prepared by using a conventional solid-state reaction process. Na_2CO_3 (99.8%), K_2CO_3 (99%) and Nb_2O_5 (99.5%) were used as the raw materials with a molar ratio of 0.585:0.535:1.0. Amounts of excessive Na (17%) and K (7%) were determined based on sintering experiments leading to a stoichiometric KNN 50/50 ceramic target. The mixed raw materials were ball-milled for 24 h using alcohol as the dispersion medium, dried, and calcined at 850 °C for 6 h in air. Then the calcined powders were mixed with a binder of 5 wt% polyvinyl butyral (PVB) and pressed into pellets with a 60 mm-diameter and an 8 mm-thickness under a uniaxial pressing @ 10 MPa in a stainless-steel die. These pellets were then sintered at 1040 °C in air for 2 h after burning of the PVB binder at 650 °C for 5 h⁶⁴. To avoid the formation of NaOH and KOH, the sintered target was kept in a vacuum cabinet.

Deposition of the KNN film

Single-crystalline substrates of (100) SrTiO_3 (STO) as well as the SrRuO_3 (SRO) ceramic target were provided by Anhui Institute of Optics and Fine Mechanics (Chinese Academy of Sciences, China). A base pressure of 2.0×10^{-4} Pa was achieved in a multi-target sputtering chamber prior to the sequential deposition of a bottom electrode (SRO) layer and a KNN film from the corresponding ceramic targets. KNN films of ~150 and ~500 nm thicknesses with a SRO layer of a fixed thickness ~60 nm were sputter-deposited in a mixed Ar/O_2 atmosphere (1.2 Pa, Ar/O_2 flow ratio = 3:1). During the sputtering process, the substrate temperature was held at 600 °C. Right after their depositions, the KNN thin film heterostructures were kept at 600 °C in 2.5 Pa pure oxygen for 20 min, to help reduce the oxygen vacancies. Metal-ferroelectric-metal (MFM) testing structures were formed after deposition of top electrodes (circular Au pads with $\phi = 200 \mu\text{m}$), which were sputtered at room temperature via a shadow mask.

Characterization

The phase structures and crystallographic orientations of the KNN films were analyzed using standard X-ray 2θ -scans (in a commercial Rigaku Dmax-2500PC, Japan) and pole figure (R-156 Axis Spider, Smart Lab Rigaku, Japan; 40 kV, 200 mA). In the X-ray pole figure measurement, the (110) KNN peak was used. The 500 nm-thick film sample was rotated by varying the tilt angle ψ from 0° to 90°, and the azimuthal angle φ from 0° to 360° for every single ψ value. Nanostructures of the films were analyzed using transmission electron microscopy (TEM, JEOL JEM-2100HR) with cross-sectional samples prepared by using a focus ion beam (FIB) milling instrument (Scios2, FEI, USA). The surface morphology of the films was investigated by using an atomic force microscope (AFM, Micro Nano D-5A, with CSC21-AIBS AFM tips from Mikro Masch). The chemical bonding states of K, Na, Nb, and O were analyzed using X-ray photoelectron spectroscopy (XPS, Thermo Scientific ESCALAB 250Xi). The ferroelectric polarization-electric field (P–E) hysteresis loops were measured by using a Radiant Precision LC ferroelectric tester (Radiant Technology, USA). The capacitance (C)–voltage (V) (C–V) tests, which were used to extract the dielectric permittivity χ -electric field E (χ -E) curves, were carried out in a TH2828S LCR bridge (Tong hui Electronics, China), by superimposing a small AC signal (V_p -p = 1 V @ 1 kHz) on a DC bias voltage sweeping from its negative maximum to its positive maximum, and vice versa.

DATA AVAILABILITY

The authors declare that the main data supporting the findings of this study are available within the paper. Other relevant data are available from the corresponding author upon reasonable request.

Received: 16 October 2020; Accepted: 23 March 2021;

Published online: 06 May 2021

REFERENCES

- Cole, M. W., Nothwang, W. D., Hubbard, C., Ngo, E. & Ervin, M. Low dielectric loss and enhanced tunability of $\text{Ba}_{0.6}\text{Sr}_{0.4}\text{TiO}_3$ based thin films via material compositional design and optimized film processing methods. *J. Appl. Phys.* **93**, 9218–9225 (2003).
- Tagantsev, A. K., Sherman, V. O., Astafev, K. F., Venkatesh, J. & Setter, N. Ferroelectric materials for microwave tunable applications. *J. Electroceram.* **11**, 5–66 (2003).
- Bao, P., Jackson, T. J., Wang, X. & Lancaster, M. J. Barium strontium titanate thin film varactors for room-temperature microwave device applications. *J. Phys. D: Appl. Phys.* **41**, 63001 (2008).
- Zhao, J. et al. Effects of Bi_2O_3 , Sm_2O_3 content on the structure, dielectric properties and dielectric tunability of BaTiO_3 ceramics. *J. Mater. Sci: Mater. Electron.* **30**, 19279–19288 (2019).
- Everhardt, A. S. et al. Temperature-independent giant dielectric response in transitional BaTiO_3 thin films. *Appl. Phys. Rev.* **7**, 011402 (2020).
- Zhang, W., Hu, F., Zhang, H. & Ouyang, J. Investigation of the electrical properties of RF sputtered BaTiO_3 films grown on various substrates. *Mater. Res. Bull.* **95**, 23–29 (2017).
- Aymen, S., Mascot, M., Jomni, F. & Carru, J. High tunability in lead-free $\text{Ba}_{0.85}\text{Sr}_{0.15}\text{TiO}_3$ thick films for microwave tunable applications. *Ceram. Int.* **45**, 23084–23088 (2019).
- Wang, F. & Ma, W. Phase stability and dielectric properties of (011) epitaxial ($\text{Ba}_{0.6}\text{Sr}_{0.4}$) TiO_3 films. *J. Appl. Phys.* **125**, 082528 (2019).
- Yuan, Z. et al. Large dielectric tunability and microwave properties of Mn-doped (Ba,Sr) TiO_3 thin films. *Appl. Phys. Lett.* **87**, 152901 (2005).
- Wu, M., Li, X., Yu, S., Sun, Y. & Dong, H. Dielectric properties of the bulk and interfacial layers in ferroelectric $\text{BaZr}_{0.2}\text{Ti}_{0.8}\text{O}_3$ thin films. *Ceram. Int.* **45**, 10917–10923 (2019).
- Zhong, S. et al. Highly tunable and temperature insensitive multilayer barium strontium titanate films. *Appl. Phys. Lett.* **90**, 092901 (2007).
- Cole, M. W., Ngo, E., Hirsch, S., Okatan, M. B. & Alpay, S. P. Dielectric properties of MgO-doped compositionally graded multilayer barium strontium titanate films. *Appl. Phys. Lett.* **92**, 072906 (2008).
- Garten, L. M. & Trolier-McKinstry, S. The field induced $e_{31,f}$ piezoelectric and Rayleigh response in barium strontium titanate thin films. *Appl. Phys. Lett.* **105**, 132905 (2014).
- Tang, X. G., Chew, K. H. & Chan, H. L. W. Diffuse phase transition and dielectric tunability of $\text{Ba}(\text{Zr}_{1-x}\text{Ti}_x)\text{O}_3$ relaxor ferroelectric ceramics. *Acta Mater.* **52**, 5177–5183 (2004).
- Mahmoud, A. E., Affy, A. S. & Parashar, S. K. S. Dielectric, tunability, leakage current, and ferroelectric properties of ($\text{K}_{0.45}\text{Na}_{0.55}$) $_{0.95}\text{Li}_{0.05}\text{NbO}_3$ lead free piezoelectric. *J. Mater. Sci: Mater. Electron.* **30**, 2659–2668 (2019).
- Yu, Z., Ang, C., Guo, R. & Bhalla, A. S. Dielectric properties and high tunability of $\text{Ba}(\text{Ti}_{0.7}\text{Zr}_{0.3})\text{O}_3$ ceramics under dc electric field. *Appl. Phys. Lett.* **81**, 1285–1287 (2002).
- Blomqvist, M., Koh, J., Khartsev, S., Grishin, A. & Andréasson, J. High-performance epitaxial $\text{Na}_{0.5}\text{K}_{0.5}\text{NbO}_3$ thin films by magnetron sputtering. *Appl. Phys. Lett.* **81**, 337–339 (2002).
- Li, T., Wang, G., Li, K., Du, G. & Chen, Y. Electrical properties of lead-free KNN films on SRO/STO by RF magnetron sputtering. *Ceram. Int.* **40**, 1195–1198 (2014).
- Li, T., Wang, G., Remiens, D. & Dong, X. Characteristics of highly (001) oriented (K, Na) NbO_3 films grown on LaNiO_3 bottom electrodes by RF magnetron sputtering. *Ceram. Int.* **39**, 1359–1363 (2013).
- Ren, P. et al. Large nonlinear dielectric behavior in $\text{BaTi}_{1-x}\text{Sn}_x\text{O}_3$. *Sci. Rep.* **7**, 6693 (2017).
- Peng, B., Fan, H., Li, Q. & Zhang, Q. Dielectric tunability properties of the $\text{Pb}[(\text{Mg}_{1/3}\text{Nb}_{2/3})_{1-x}\text{Zr}_x]\text{O}_3$ ceramics. *J. Alloy. Compd.* **549**, 283–287 (2013).
- Fujii, I. et al. Fabrication of (K,Na) NbO_3 films on $\text{SrRuO}_3/(001)\text{SrTiO}_3$ substrates by pulsed laser deposition. *Jpn. J. Appl. Phys.* **54**, 10NA13 (2015).
- Fujii, I., Yamauchi, T., Imai, T., Adachi, H. & Wada, T. Ferroelectric properties of (Li,K,Na) NbO_3 epitaxial films fabricated by pulsed laser deposition. *Jpn. J. Appl. Phys.* **53**, 09PA09 (2014).
- Ito, Y. et al. Growth of epitaxial (K,Na) NbO_3 films with various orientations by hydrothermal method and their properties. *Jpn. J. Appl. Phys.* **58**, SLLB14 (2019).
- Khartsev, S., Grishin, A., Andréasson, J., Koh, J. & Song, J. Comparative characteristics of $\text{Na}_{0.5}\text{K}_{0.5}\text{NbO}_3$ films on Pt by pulsed laser deposition and magnetron sputtering. *Integr. Ferroelectr.* **55**, 769–779 (2010).
- Chen, L., Nagarajan, V., Ramesh, R. & Roytburd, A. L. Nonlinear electric field dependence of piezoresponse in epitaxial ferroelectric lead zirconate titanate thin films. *J. Appl. Phys.* **94**, 5147–5152 (2003).

27. Li, T. et al. Influence of LNO top electrodes on electrical properties of KNN/LNO thin films prepared by RF magnetron sputtering. *J. Am. Ceram. Soc.* **96**, 787–790 (2012).
28. Li, G. et al. Effects of excess amount of K and Na on properties of $(K_{0.48}Na_{0.52})NbO_3$ thin films. *Ceram. Int.* **38**, S279–S281 (2012).
29. Bell, A. J. Phenomenologically derived electric field-temperature phase diagrams and piezoelectric coefficients for single crystal barium titanate under fields along different axes. *J. Appl. Phys.* **89**, 3907–3914 (2001).
30. Huang, Y. H. et al. Thermodynamic and phase-field studies of phase transitions, domain structures, and switching for $Ba(Zr_xTi_{1-x})O_3$ solid solutions. *Acta Mater.* **186**, 609–615 (2020).
31. Jiang, Q. & Qiu, J. H. The thickness dependence of ferroelectric and magnetic properties in epitaxial $BiFeO_3$ thin films. *J. Appl. Phys.* **99**, 103901 (2006).
32. Winchester, B., Wu, P. & Chen, L. Q. Phase-field simulation of domain structures in epitaxial $BiFeO_3$ films on vicinal substrates. *Appl. Phys. Lett.* **99**, 052903 (2011).
33. Zhang, J. X. et al. Computer simulation of ferroelectric domain structures in epitaxial $BiFeO_3$ thin films. *J. Appl. Phys.* **103**, 094111 (2008).
34. Mtebwa, M., Tagantsev, A. K. & Setter, N. Effect of elastic compliances and higher order Landau coefficients on the phase diagram of single domain epitaxial $Pb(Zr, Ti)O_3$ (PZT) thin films. *Aip Adv.* **4**, 127150 (2014).
35. Zhou, M., Wang, J., Chen, L. & Nan, C. Strain, temperature, and electric-field effects on the phase transition and piezoelectric responses of $K_{0.5}Na_{0.5}NbO_3$ thin films. *J. Appl. Phys.* **123**, 154106 (2018).
36. Zhao, X., Wang, J. & Chen, L. A thermodynamic study of phase transitions and electrocaloric properties of $K_{0.5}Na_{0.5}NbO_3$ single crystals. *Appl. Phys. Lett.* **116**, 092902 (2020).
37. Liu, D., Bai, G. & Gao, C. Phase diagrams classification based on machine learning and phenomenological investigation of physical properties in $K_{1-x}Na_xNbO_3$ thin films. *J. Appl. Phys.* **127**, 154101 (2020).
38. Wang, J. J., Wu, P. P., Ma, X. Q. & Chen, L. Q. Temperature-pressure phase diagram and ferroelectric properties of $BaTiO_3$ single crystal based on a modified Landau potential. *J. Appl. Phys.* **108**, 114105 (2010).
39. Qiu, J. H., Zhao, T. X., Chen, Z. H., Yuan, N. Y. & Ding, J. N. Orientation dependence of phase diagrams and physical properties in epitaxial $Ba_{0.6}Sr_{0.4}TiO_3$ films. *Solid. State Commun.* **272**, 57–62 (2018).
40. Peng, J. et al. A thermodynamic potential for barium zirconate titanate solid solutions. *Npj. Comput. Mater.* **4**, 1–9 (2018).
41. Li, H. et al. Dependence of dielectric properties on internal stresses in epitaxial barium strontium titanate thin films. *Appl. Phys. Lett.* **78**, 2354–2356 (2001).
42. Kim, D. H., Lee, H. N., Biegalski, M. D. & Christen, H. M. Effect of epitaxial strain on ferroelectric polarization in multiferroic $BiFeO_3$ films. *Appl. Phys. Lett.* **92**, 012911 (2008).
43. Luo, J. et al. Domain evolution and piezoelectric response across thermotropic phase boundary in $(K,Na)NbO_3$ -based epitaxial thin films. *ACS Appl. Mater. Inter.* **9**, 13315–13322 (2017).
44. Luo, J. et al. Monoclinic $(K,Na)NbO_3$ ferroelectric phase in epitaxial films. *Adv. Electron. Mater.* **3**, 1700226 (2017).
45. von Helden, L. et al. Huge impact of compressive strain on phase transition temperatures in epitaxial ferroelectric $K_xNa_{1-x}NbO_3$ thin films. *Appl. Phys. Lett.* **114**, 232905 (2019).
46. Shiraiishi, T. et al. Structural and electrical characterization of hydrothermally deposited piezoelectric $(K,Na)(Nb,Ta)O_3$ thick films. *J. Mater. Sci.* **55**, 8829–8842 (2020).
47. Blochl, P. E. Projector augmented-wave method. *Phys. Rev. B: Condens Matter* **50**, 17953–17979 (1994).
48. Kresse, G. & Joubert, D. From ultrasoft pseudopotentials to the projector augmented-wave method. *Phys. Rev. B* **59**, 1758–1775 (1999).
49. Perdew, J. P., Burke, K. & Ernzerhof, M. Generalized gradient approximation made simple. *Phys. Rev. Lett.* **77**, 3865–3868 (1996).
50. Wang, K. & Li, J. F. Analysis of crystallographic evolution in $(Na,K)NbO_3$ -based lead-free piezoceramics by x-ray diffraction. *Appl. Phys. Lett.* **91**, 262902 (2007).
51. Yu, Q., Zhu, F., Cheng, L., Wang, K. & Li, J. Determination of crystallographic orientation of lead-free piezoelectric $(K,Na)NbO_3$ epitaxial thin films grown on $SrTiO_3(100)$ surfaces. *Appl. Phys. Lett.* **104**, 102902 (2014).
52. Akmal, M. H. M., MWarikh, A. R. & Ralib, A. A. M. Vibrational piezoelectric energy harvester's performance using PZT vs KNN. *Mater. Res. Express* **6**, 115708 (2019).
53. Wang, L., Ren, W., Shi, P. & Wu, X. Cobalt doping effects on structures and electrical properties of lead-free ferroelectric $K_{0.5}Na_{0.5}NbO_3$ films. *J. Alloy. Compd.* **608**, 202–206 (2014).
54. Wang, L., Ren, W., Shi, P. & Wu, X. Structures, electrical properties, and leakage current behaviors of un-doped and Mn-doped lead-free ferroelectric $K_{0.5}Na_{0.5}NbO_3$ films. *J. Appl. Phys.* **115**, 034103 (2014).
55. Wang, L., Yao, K., Goh, P. C. & Ren, W. Volatilization of alkali ions and effects of molecular weight of polyvinylpyrrolidone introduced in solution-derived ferroelectric $K_{0.5}Na_{0.5}NbO_3$ films. *J. Mater. Res.* **24**, 3516–3522 (2009).
56. Wang, L. et al. Effect of pyrolysis temperature on $K_{0.5}Na_{0.5}NbO_3$ thick films derived from polyvinylpyrrolidone-modified chemical solution. *J. Am. Ceram. Soc.* **93**, 3686–3690 (2010).
57. Xu, L. et al. Fabrication of the transparent ferroelectric heterostructures based on KNN-based lead-free films. *J. Phys. D: Appl. Phys.* **53**, 415301 (2020).
58. Zhang, Y. et al. Strain engineered $CaBi_2Nb_2O_9$ thin films with enhanced electrical properties. *ACS Appl. Mater. Inter.* **8**, 16744–16751 (2016).
59. Niu, M. et al. Integration-friendly, chemically stoichiometric $BiFeO_3$ films with a piezoelectric performance challenging that of PZT. *ACS Appl. Mater. Inter.* **12**, 33899–33907 (2020).
60. Kizaki, Y., Noguchi, Y. & Miyayama, M. Defect control for low leakage current in $K_{0.5}Na_{0.5}NbO_3$ single crystals. *Appl. Phys. Lett.* **89**, 142910 (2006).
61. Wang, L. et al. Enhanced ferroelectric properties in Mn-doped $K_{0.5}Na_{0.5}NbO_3$ thin films derived from chemical solution deposition. *Appl. Phys. Lett.* **97**, 072902 (2010).
62. Zhang, W. et al. Space-charge dominated epitaxial $BaTiO_3$ heterostructures. *Acta Mater.* **85**, 207–215 (2015).
63. Wang, X. et al. Growth and field dependent dielectric properties of epitaxial $Na_{0.5}K_{0.5}NbO_3$ thin films. *Appl. Phys. Lett.* **73**, 927–929 (1998).
64. Huan, Y., Wang, X. & Li, L. Displacement of Ta-O bonds near polymorphic phase transition in Li-, Ta-, and Sb-modified $(K, Na)NbO_3$ ceramics. *Appl. Phys. Lett.* **104**, 242905 (2014).

ACKNOWLEDGEMENTS

The authors are deeply grateful for the financial support from the National Natural Science Foundation of China (NSFC) (Grant Nos. 51772175, 52072150, 51702119), the seed funding for top talents in Qilu University of Technology (Shandong Academy of Sciences), the international cooperation research project of Qilu University of Technology (QLUTGJHZ2018003). Y.H. acknowledges the Young Elite Scientists Sponsorship Program by CAST. H.C. acknowledges the support from the Jiangsu Province NSFC (Grant No. BK20180764). J.O. would also like to acknowledge the support from the Independent Innovation Foundation of Shandong University (Grant Nos. 2018JC045, 2017ZD008, and 2015JC034).

AUTHOR CONTRIBUTIONS

L.H., Y.H., and J.O. designed the whole study. L.H. performed the research, collected and analyzed the data, and wrote the draft. Y.Y. and W.R. carried out the DFT study. J.O. analyzed and discussed the data, and revised the manuscript. Y.H. helped prepare the KNN target. H.C., Y.-Y.Z., Y.W., and J.Y. helped collect experimental data and participated in the discussion.

COMPETING INTERESTS

The authors declare no competing interests.

ADDITIONAL INFORMATION

Correspondence and requests for materials should be addressed to Y.Y., Y.H. or J.O.

Reprints and permission information is available at <http://www.nature.com/reprints>

Publisher's note Springer Nature remains neutral with regard to jurisdictional claims in published maps and institutional affiliations.



Open Access This article is licensed under a Creative Commons Attribution 4.0 International License, which permits use, sharing, adaptation, distribution and reproduction in any medium or format, as long as you give appropriate credit to the original author(s) and the source, provide a link to the Creative Commons license, and indicate if changes were made. The images or other third party material in this article are included in the article's Creative Commons license, unless indicated otherwise in a credit line to the material. If material is not included in the article's Creative Commons license and your intended use is not permitted by statutory regulation or exceeds the permitted use, you will need to obtain permission directly from the copyright holder. To view a copy of this license, visit <http://creativecommons.org/licenses/by/4.0/>.

© The Author(s) 2021